Aperture-Coupled Thin-Film Superconducting Meander Antennas

Hanyang Y. Wang and Michael J. Lancaster

***Abstract*—A thin-film superconducting meander patch antenna coupled by an H-shaped aperture is proposed. It is analyzed using a full wave electromagnetic simulator and the theory of cavity model for microstrip patch antennas. The meander patch was fabricated from a single-sided film of YBCO ($YBa_2Cu_3O_7$) on MgO with a typical transition temperature of 90 K. Simulated results are presented for return loss, radiation pattern, and efficiency and these are shown in good agreement with the results obtained from network analyzer measurements. An array of a number of elements is also proposed for wide-band operation.**

***Index Terms*—Patch antennas, superconducting antennas.**

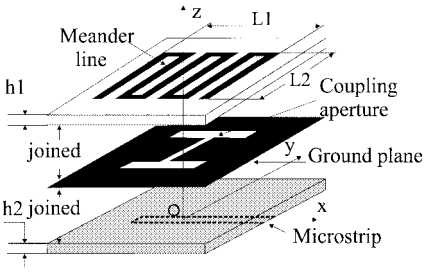

Fig. 1. Geometry of aperture-coupled meander antenna.

I. Introduction

THE dimensions of conventional patch antennas are normally around a half waveguide wavelength. In some applications, the space occupied by antenna arrays may become too large and it is often desirable to miniaturize patch antennas. There are a number of effective ways to reduce the size of patch antennas: 1) increase electrical length by optimizing the shape of a patch; 2) use high-permittivity substrates; 3) introduce shorting pins at the edge of the patch or in the vicinity of a coaxial feed; and 4) a combination of these approaches. An H-shaped patch antenna proposed by Palanisamy and Gary is one of the well-known choices for miniaturization of patch antennas by optimizing the shape [1]. The dimensions of the H-shaped patch antenna are normally about a quarter waveguide wavelength square. The radiation efficiency of the H-shaped patch antenna drops significantly due to the conductor loss, which is the common disadvantage of small antennas.

To increase radiation efficiency, high-temperature superconductors (HTS) are often used in the fabrication of small antennas [2]–[5]. Chaloupka investigated a HTS H-shaped patch antenna and presented numerical and experimental results [6], [7]. A more compact antenna is the meander antenna proposed and analyzed by Bando and Yamauchi [8] and Esa and Lancaster [9]. However, these H-shaped patch and meander antennas are fed by coaxial cable or coplanar strips which are not adequate for antenna array applications. An aperture-coupled H-shaped patch antenna has been examined in [10].

Manuscript received May 28, 1998; revised September 15, 1998. This work was supported by the Engineering and Physical Science Council of the U.K. M. J. Lancaster would like to thank the Nuffield Foundation for their support.

The authors are with the School of Electronic and Electrical Engineering, University of Birmingham, Edgbaston, Birmingham B15 2TT, U.K.

Publisher Item Identifier S 0018-926X(99)04827-9.

In this paper, an aperture-coupled HTS meander patch antenna is proposed and analyzed. The meander antenna is fed by a microstrip open end through an H-shaped aperture in the intervening ground plane. The aperture-coupled feeding structure can be easily realized in the design of antenna arrays. The dimension of the meander patch with three meander sections is less than one eighth of waveguide wavelength, while its radiation patterns are basically the same as those of conventional rectangular patches. The properties of the proposed meander antennas are examined both numerically and experimentally using a full wave electromagnetic simulator, theory of cavity model for microstrip antennas and a microwave network analyzer. Good agreement between simulated results and measured results is demonstrated.

II. Principle of Meander Patch Antennas

The geometry of the aperture-coupled meander patch antenna with three meander sections is illustrated in Fig. 1, where the meander section is defined as the bend of the meander line at the side without open ends. The structure consists of two substrates separated by a ground plane. A microstrip open end is on the bottom side of the lower substrate, whereas the meander patch is on the top side of the upper substrate. They are coupled by an H-shaped aperture on the ground plane. The coupling aperture was chosen as H shape so that the aperture can be covered by the meander patch so as to reduce undesirable radiation from the aperture; it can also ease the positioning constraints for array applications [11]. The match between the feed and the patch can be achieved by choosing and adjusting the parameters of the substrates, the width and length of the microstrip open end, the size of the coupling aperture, and, most importantly, the offset of the patch in respect to the center of the coupling aperture.

The lowest resonance of the meander antenna occurs when the total length of the meander line is approximately a half

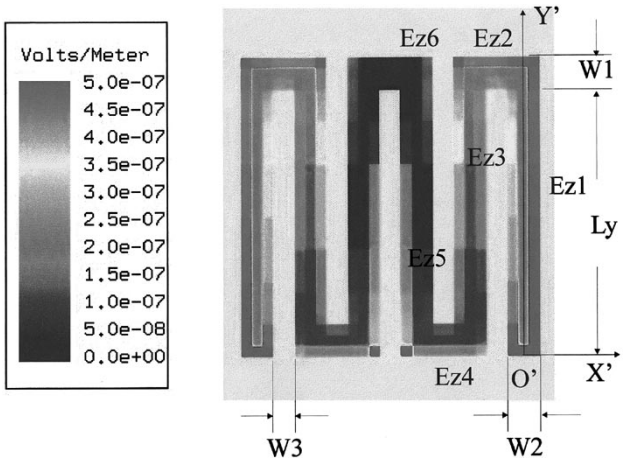

(a)

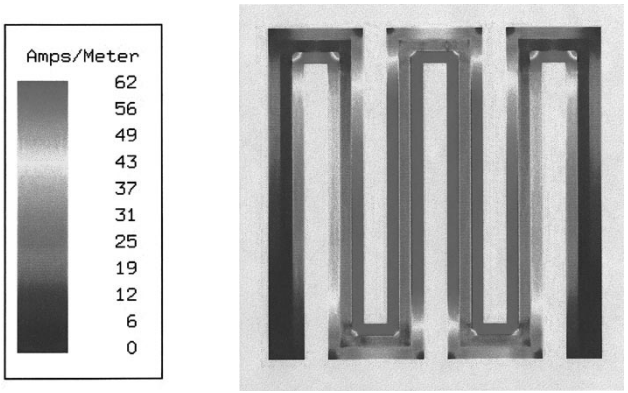

(b)

Fig. 2. (a) Charge distribution simulated by Sonnet. (b) Current distribution simulated by Sonnet.

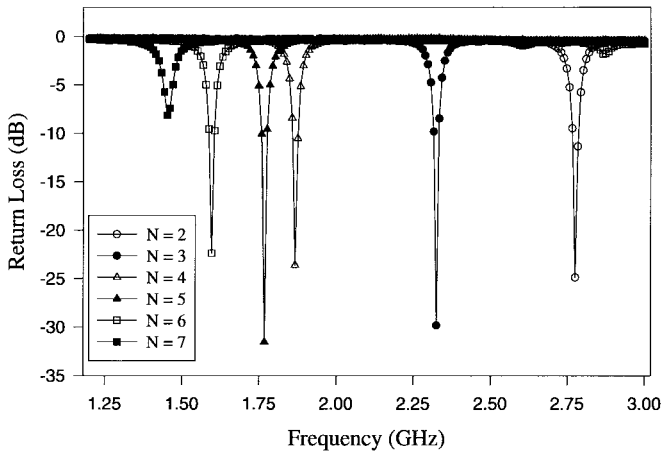

Fig. 3. Return loss as a function of frequency.

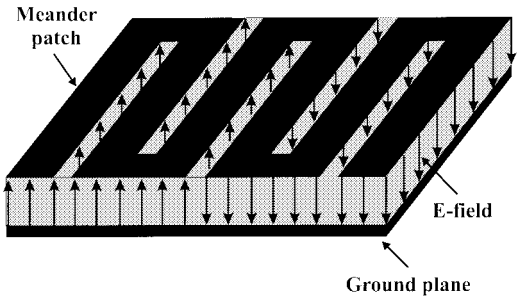

Fig. 4. E-field distribution in cavity model.

waveguide wavelength. The simulated charge and current distributions on the meander line using the full wave simulator Sonnet em [12] are shown in Fig. 2. The currents on the horizontal segments (parallel to x' axis) of the meander line have same direction and, hence, they behave as a number of radiation elements (five in this case) constructing a dipole in horizontal direction. On the other hand, the directions of currents on any two symmetrically vertical segments (parallel to y' axis) are opposite, which has much lower contribution to the desired radiation field. For the meander patch with three sections, the size $L1$ of a square meander patch ($L1 = L2$) is between $1/8$ and $1/12$ of waveguide wavelength depending on the width of meander line and the distance between meander lines. For a fixed overall size, the resonant frequency of the meander patch drops with the increment of the meander sections. The measured return loss for various meander sections is shown in Fig. 3, where the overall size is $L1 \times L2 = 8.0 \times 5.0$ (mm)^2 and the width of the meander line is 0.5 mm. As can be seen, the resonant frequency of the meander antennas decreases substantially from 2.75 GHz to 1.50 GHz with the increment of the meander section from two to seven, and all of the antennas are well matched except for that with seven meander sections. The advantage of the meander antenna over the H-shaped antenna is that it can be arbitrarily shrunk in size for a given frequency. However, too many meander sections for a given substrate thickness result in lower radiation efficiency and for a given area cause a higher level of cross polarization. The meander antenna can also resonate when the total length of the meander line equals one or more than one waveguide wavelength, which represents higher resonance.

III. Cavity Model for Analyzing Meander Patch

It is well known that the cavity model [13] is convenient and relatively accurate approach for the analysis of microstrip patch antennas and it has been successfully applied to many kinds of microstrip patches, such as rectangular, circular, and triangular patches. Here, it is employed to examine the meander patch antenna. The equivalent cavity model for the meander patch is illustrated in Fig. 4, in which it is assumed that electric field is normal to the ground plane because of the thin substrate. The top wall (meander line) and the bottom walls (ground plane) of the cavity are electric wall while all of the side walls along the meander line are magnetic wall. The radiation field of the cavity can be calculated using electric potential if the equivalent magnetic current, z component of electric field, on the magnetic walls is available. Based on the charge distribution obtained from the full wave simulator *em* as shown in Fig. 2, the z component of electric field along longitudinal direction of the meander line is approximately a sinusoidal distribution, whereas the transverse distribution of the magnetic current along the meander line can be approximated using a polynomial function. The general

form of the segment n of magnetic $E_{zn}(x',y')$ current in the horizontal direction at the local coordinate system $x'-0'-y'$ defined in Fig. 2 is given by

$$\begin{aligned} E_{zn}(x',y') &= \sin(b_{xn0}+b_{xn1}x')\cdot(a_{xn0}+a_{xn1}y'+a_{xn2}y'^2) \\ a_{xn0} &= A_{xnm} \\ a_{xn1} &= \frac{A_{xnu}-A_{xnl}}{W_1} \\ a_{xn2} &= 2\cdot\frac{A_{xnu}+A_{xnl}-2A_{xnm}}{W_1^2}. \end{aligned} \tag{1}$$

Similarly, the general form of the segment n of magnetic current $E_{zn}(x',y')$ in the vertical direction is given by

$$\begin{aligned} E_{zn}(x',y') &= \sin(b_{yn0}+b_{yn1}y')\cdot(a_{yn0}+a_{yn1}x'+a_{yn2}x'^2) \\ a_{yn0} &= A_{ynm} \\ a_{yn1} &= \frac{A_{ynr}-A_{ynl}}{W_2} \\ a_{yn2} &= 2\cdot\frac{A_{ynr}+A_{ynl}-2A_{ynm}}{W_2^2} \end{aligned} \tag{2}$$

where b_{xn0}, b_{xn1}, b_{yn0}, and b_{yn1} are coefficients, which can be readily obtained by assuming the electric field E_z distribution along the meander line is sinusoidal; A_{ynl}, A_{ynm}, and A_{ynu} are the values of the z component of the electric field at the low edge, the middle, and the up edge of the meander line; A_{xnl}, A_{xnm}, and A_{xnr} are the values of the z component of the electric field at the left edge, the middle, and the right edge of the meander line, which can be obtained from the simulated charge distribution; W_1 and W_2 are the width of the meander line as shown in Fig. 2. Typically, the segment of magnetic current $E_{z1}(x',y')$ as shown in Fig. 2 is given by

$$\begin{aligned} E_{z1}(x',y') &= \sin\left[\frac{\pi\cdot(0.5L-y')}{L}\right] \\ &\quad\cdot(a_{y10}+a_{y11}x'+a_{y12}x'^2) \\ a_{y10} &= A_{y1m} \\ a_{y11} &= \frac{A_{y1r}-A_{y1l}}{W_2} \\ a_{y12} &= 2\cdot\frac{A_{y1r}+A_{y1l}-2A_{y1m}}{W_2^2} \end{aligned} \tag{3}$$

where L is the total length of the meander line. The values of A_{y1l}, A_{y1m}, and A_{y1r} are 0.65, 0.35, and 1.0, respectively, based on the simulated results obtained from the full wave simulator *em* and the radiation pattern and efficiency are not extremely sensitive to these values.

The electric potential at a point $\vec{r}$ can be expressed in terms of magnetic current and Green's function, namely

$$\vec{F}(\vec{r}) = \frac{\varepsilon_0}{2\pi}\iint[\vec{n}\times\vec{E}(\vec{r}_0)]\frac{\exp(-jk_0|\vec{r}-\vec{r}_0|)}{|\vec{r}-\vec{r}_0|}\,dS_0 \tag{4}$$

where $\vec{r}$ denotes field point and $\vec{r}_0$ denotes source point. This integration is around all of the side walls of the meander line cavity. Electric and magnetic fields in far-field zone are then given by

$$\begin{aligned} \vec{H}(\vec{r}) &= -j\omega\vec{F}(\vec{r}) \\ E_\theta(\vec{r}) &= \sqrt{\frac{\mu_0}{\varepsilon_0}}H_\phi(\vec{r}) \\ E_\phi(\vec{r}) &= -\sqrt{\frac{\mu_0}{\varepsilon_0}}H_\theta(\vec{r}) \end{aligned} \tag{5}$$

where H_ϕ and H_θ are the components of magnetic field in spherical coordinate system and they can be expressed in terms of the components in Cartesian coordinate, namely

$$\begin{aligned} H_\theta(r,\theta,\phi) &= H_x(r,\theta,\phi)\cos(\phi)\cos(\theta) \\ &\quad + H_y(r,\theta,\phi)\sin(\phi)\cos(\theta) \\ H_\phi(r,\theta,\phi) &= -H_x(r,\theta,\phi)\sin(\phi) + H_y(r,\theta,\phi)\cos(\phi). \end{aligned} \tag{6}$$

Since the meander patch is symmetrical to y axis, only half of the meander patch ($x>0$) needs to be examined. For far-field zone where $|\vec{r}| \gg |\vec{r}_0|$, if the electric field $E_z(\vec{r}_0)$ is homogenous along z direction the x component of magnetic far-field radiated by nth segment of magnetic current at y_0 (y_0 is a constant) ranging from x_{n1} to x_{n2} is given by

$$\begin{aligned} H_x^n(\vec{r}) &= -j\omega F_x(\vec{r}) \\ &= -\frac{j\omega\varepsilon_0}{2\pi}\iint E_z(x_0,y_0)\cdot\frac{\exp(-jk_0|\vec{r}-\vec{r}_0|)}{|\vec{r}-\vec{r}_0|}\,dx_0\,dz_0 \\ &= \frac{2\omega\varepsilon_0}{r\pi}\exp[-jk_0(r-y_0\sin(\theta)\sin(\phi))] \\ &\quad\cdot\frac{\sin\left(k_0\cos(\theta)\frac{h_1}{2}\right)}{k_0\cos(\theta)}\cdot\int_{x_{n1}}^{x_{n2}}E_z(x_0) \\ &\quad\times\sin(k_0x_0\sin(\theta)\cos(\phi))\,dx_0. \end{aligned} \tag{7}$$

Substituting (1) into (7) and evaluating the resultant equation give

$$\begin{aligned} &H_x^n(\vec{r}) \\ &= \frac{2\omega\varepsilon_0}{r\pi}\exp[-jk_0(r-y_0\sin(\theta)\sin(\phi))] \\ &\quad\cdot\frac{\sin\left(k_0\cos(\theta)\frac{h_1}{2}\right)}{k_0\cos(\theta)}\cdot\left(A_{xn0}+A_{xn1}y_0+A_{xn2}y_0^2\right) \\ &\quad\cdot\{[F1(x_{n2},b_{xn0},b_{xn1},C_x)-F1(x_{n1},b_{xn0},b_{xn1},C_x)] \\ &\quad+[F2(x_{n2},b_{xn0},b_{xn1},C_x)-F2(x_{n1},b_{xn0},b_{xn1},C_x)]\}. \end{aligned} \tag{8}$$

Similarly, the y component of magnetic far-field radiated by nth segment of magnetic current at x_0 (x_0 is a constant) ranging from y_{n1} to y_{n2} is given by

$$\begin{aligned} H_y^n(\vec{r}) &= -j\omega F_y(\vec{r}) \\ &= \frac{j\omega\varepsilon_0}{2\pi}\iint E_z(x_0,y_0)\cdot\frac{\exp(-jk_0|\vec{r}-\vec{r}_0|)}{|\vec{r}-\vec{r}_0|}\,dy_0\,dz_0 \\ &= \frac{2j\omega\varepsilon_0}{r\pi}\exp(-jk_0r)\cdot\cos(k_0x_0\sin(\theta)\cos(\phi)) \\ &\quad\times\frac{\sin\left(k_0\cos(\theta)\frac{h_1}{2}\right)}{k_0\cos(\theta)}\cdot\int_{y_{n1}}^{y_{n2}}E_z(y_0) \\ &\quad\times\exp[jk_0y_0\sin(\theta)\sin(\phi)]\,dy_0. \end{aligned} \tag{9}$$

After evaluating the above integral, we obtain

$$
\begin{aligned}
&H_y^n(\vec{r}) \\
&\quad = \frac{2j\omega\varepsilon_0}{r\pi}\exp(-jk_0r)\cdot\cos(k_0x_0\sin(\theta)\cos(\phi)) \\
&\qquad \times \frac{\sin\left(k_0\cos(\theta)\frac{h_1}{2}\right)}{k_0\cos(\theta)}\cdot\left(a_{yn0}+a_{yn1}x_0+a_{yn2}x_0^2\right) \\
&\qquad \times \{j[F1(y_{n2},b_{yn0},b_{yn1},C_y)-F1(y_{n1},b_{yn0},b_{yn1},C_y)] \\
&\qquad + j[F2(y_{n2},b_{yn0},b_{yn1},C_y)-F2(y_{n1},b_{yn0},b_{yn1},C_y)] \\
&\qquad + [F3(y_{n2},b_{yn0},b_{yn1},C_y)-F3(y_{n1},b_{yn0},b_{yn1},C_y)] \\
&\qquad + [F4(y_{n2},b_{yn0},b_{yn1},C_y)-F4(y_{n1},b_{yn0},b_{yn1},C_y)]\}
\end{aligned}
\tag{10}
$$

where

$$
\begin{aligned}
C_x &= k_0\sin(\theta)\cos(\phi) \\
C_y &= k_0\sin(\theta)\sin(\phi)
\end{aligned}
$$

$$
\begin{aligned}
&F1(u,A,B,C) \\
&\quad = \cos(A)\cdot\left\{\frac{\sin[(C-B)u]}{2(C-B)}-\frac{\sin[(C+B)u]}{2(C+B)}\right\} \\
&F2(u,A,B,C) \\
&\quad = \sin(A)\cdot\left\{-\frac{\cos[(C-B)u]}{2(C-B)}-\frac{\cos[(C+B)u]}{2(C+B)}\right\} \\
&F3(u,A,B,C) \\
&\quad = \cos(A)\cdot\left\{\frac{\cos[(C-B)u]}{2(C-B)}-\frac{\cos[(C+B)u]}{2(C+B)}\right\} \\
&F4(u,A,B,C) \\
&\quad = \sin(A)\cdot\left\{\frac{\sin[(C-B)u]}{2(C-B)}-\frac{\sin[(C+B)u]}{2(C+B)}\right\}.
\end{aligned}
$$

In the above equations, k_0 is the wave number in free-space and h_1 is the thickness of the meander patch. The total radiation field is the superposition of the fields produced by all of the segments of the magnetic current sources on the side walls of the equivalent cavity, namely

$$
\begin{aligned}
H_x(\vec{r}) &= \sum_{n=1}^{N_x} H_x^n(\vec{r}) \\
H_y(\vec{r}) &= \sum_{n=1}^{N_y} H_y^n(\vec{r})
\end{aligned}
\tag{11}
$$

where N_x and N_y is the number of x-directed and y-directed magnetic currents, respectively. The radiation field in the spherical coordinate can be readily obtained by substituting the above equations into (6).

As a small antenna, the efficiency of the meander patch is a very important parameter besides its radiation pattern. The dissipation of input power to antennas is attributed to the power radiated P_r, the power dissipated in the conductor P_c and in the dielectric P_d. The loss of surface wave can be ignored if the thickness of the substrate is less than about a tenth of a free-space wavelength [13]. These parameters can be calculated from the magnetic current or electric field within the equivalent cavity and they are given by

$$
\begin{aligned}
P_r = \frac{1}{4\eta_0}\int_0^{2\pi}\int_0^{\pi}[&|E_\theta(r,\theta,\phi)^2 \\
&+ E_\phi(r,\theta,\phi)^2|]r^2\sin(\theta)\,d\theta\,d\phi
\end{aligned}
\tag{12}
$$

$$
P_c = \frac{R_s\varepsilon_r}{\eta_0^2}\iint|E_z(X_0,y_0)|^2\,dS_0 \tag{13}
$$

$$
P_d = \frac{\tan\delta\omega\varepsilon_0\varepsilon_r}{2}\iiint|E_z(x_0,y_0)|^2\,dV_0 \tag{14}
$$

where R_s is surface impedance of the conductor, $\tan\delta$ is loss tangent of the substrate material, and η_0 is wave impedance in free-space. The efficiency of the antenna is simply given by

$$
e = \frac{P_r}{P_r+P_c+P_d}. \tag{15}
$$

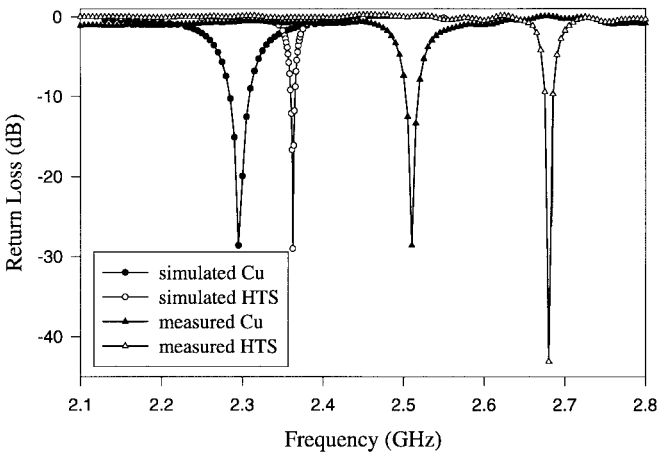

Fig. 5. Return loss as a function of frequency.

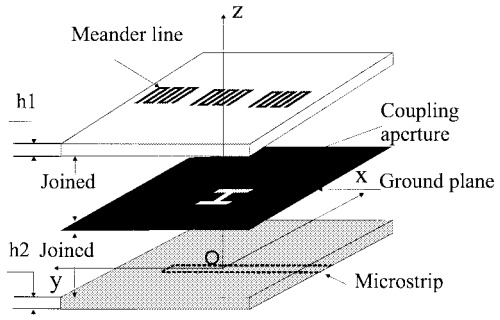

Fig. 6. Three-elements meander patch antenna.

IV. Results and Discussions

A number of copper and HTS meander patch antennas have been made. For the copper antenna, both of the meander patch and the microstrip feed were fabricated on RT/Duroid substrates ($h_1 = h_2 = 1.27$ mm, $\varepsilon_r = 10.8$). For the HTS antenna, the meander patch was fabricated from a single-side film of YBCO ($YBa_2Cu_3O_7$) on MgO substrate ($h_1 = 1.00$ mm, $\varepsilon_r = 9.8$) with a typical transition temperature of 90 K and the microstrip feed is exactly the same as the copper antenna. The meander patch is a square patch with dimensions $L1 \times L2 = 5.5 \times 5.5$ (mm)^2. The width of the meander line

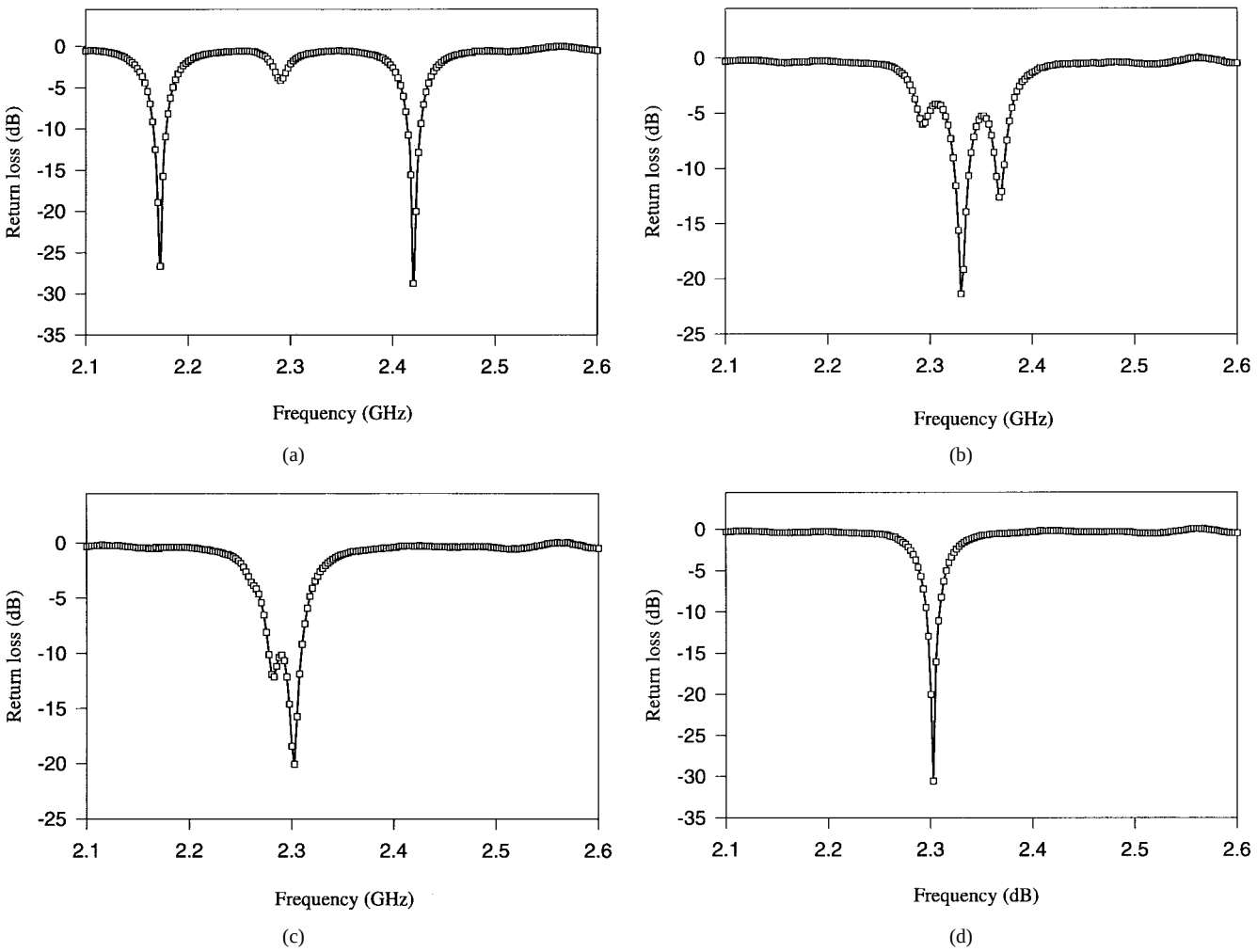

Fig. 7. Return loss against frequency for three-elements array. (a) $S = 1.0$ mm. (b) $S = 3.0$ mm. (c) $S = 3.5$ mm. (d) $S = 5.0$ mm.

is $W_1 = W_2 = 0.5$ mm and the distance between two lines W_3 is also 0.5 mm.

Fig. 5 shows the return loss as a function of frequency for the copper and HTS patch antennas obtained from the simulations and network analyzer measurements. The resonant frequency for the HTS antenna is slightly higher than that of the copper antenna because the dielectric used in the two patches is different. It was observed during the measurements that the gap between the patch and the ground plane could shift the resonant frequency up and it is practically very difficult to make the two substrates have a perfect contact. The gap could reduce the effective dielectric constant of the patch, and this is why the measured resonant frequencies are slightly higher than that of the simulated results. Not surprisingly, the bandwidth of the meander antenna is very narrow. The 3-dB bandwidth of the copper meander antenna is about 1.45% and 10-dB bandwidth is about 0.72%. For the HTS meander antenna, the 3- and 10-dB bandwidth are 1.10% and 0.50%, respectively.

The bandwidth can be increased by using parasitic radiation elements. Here, three identical meander patches are used and they are lined up in the direction paralleling the microstrip feed line as shown in Fig. 6. The meander patch in the middle is excited by the aperture on the ground plane while the two other patches are parasitically excited. The measured return loss of the copper meander antenna with parasitic patches is shown in Fig. 7, where S denotes the separation between the meander patches. When the separation value is small there exists three resonant frequencies. As the separation value increases the resonant frequencies become closer and at a certain separation value the resonant frequencies come together. The 3-dB bandwidth is about 4.3% when $S = 3.0$ mm, and the 10-dB bandwidth is about 2.0% when $S = 3.5$ mm, which are nearly three times the width of the meander antenna with a single meander patch. As the separation value increases further and the mutual couplings become weaker the meander antenna behaves like the meander antenna with a single meander patch. The radiation pattern of the three-elements array in H-plane (y-o-z plane) is the same as that of a single-element meander antenna, and in E-plane (x-o-z plane) the radiation pattern is slightly narrower than that of the single-element meander antenna since the spacing between these elements are much less than a half wavelength in free-space.

The radiation patterns of copolarization for the meander patch have been computed based on the cavity model as described in the previous section and compared with an H-shaped patch and a conventional square patch also obtained from the cavity model. The size of the H-shaped patch and the square patch is chosen so that their resonant frequency is

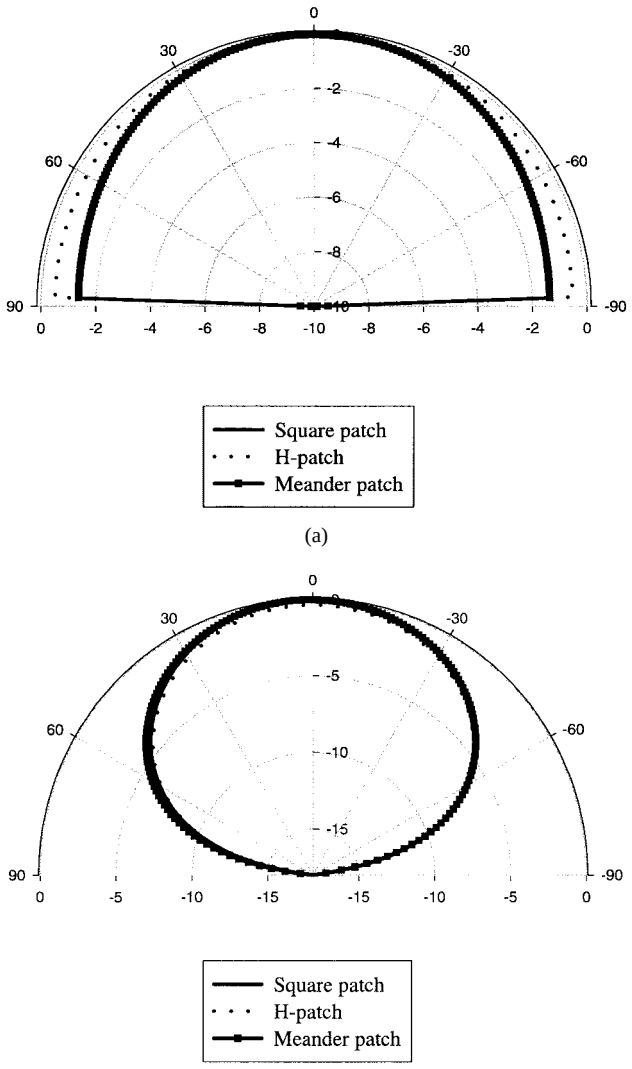

Fig. 8. (a) E-plane of radiation pattern obtained from cavity model. (b) H-plane of radiation pattern obtained from cavity model.

approximately the same as that of the meander patch (around 2.35 GHz). The dimensions of the H-shaped patch are 11.0 $\times$ 11.0 $(\text{mm})^2$ while those of square patch are 20.0 $\times$ 20.0 $(\text{mm})^2$. The computed radiation patterns for the three patches are shown in Fig. 8. It can be seen that the E-plane of the meander patch is almost the same as that of the square patch and slightly narrower than that of the H-shaped patch while the H-plane of the three patch antennas are almost the same. Fig. 9 shows the measured radiation patterns for the three patch antennas. The measurement setup for the radiation pattern is the same as that in [3]. As predicated by the cavity model, there is not much difference between the measured radiation patterns produced by the these antennas. Based on the calculation of the meander patch, the level of the cross polarization is 30 dB lower than that of the copolarization, but in the measurement it was observed that the difference between cross polarization and copolarization is about 10 dB.

The radiation efficiencies of these antennas have been examined theoretically using the cavity model and experimentally based on the measurement of antenna radiation patterns and

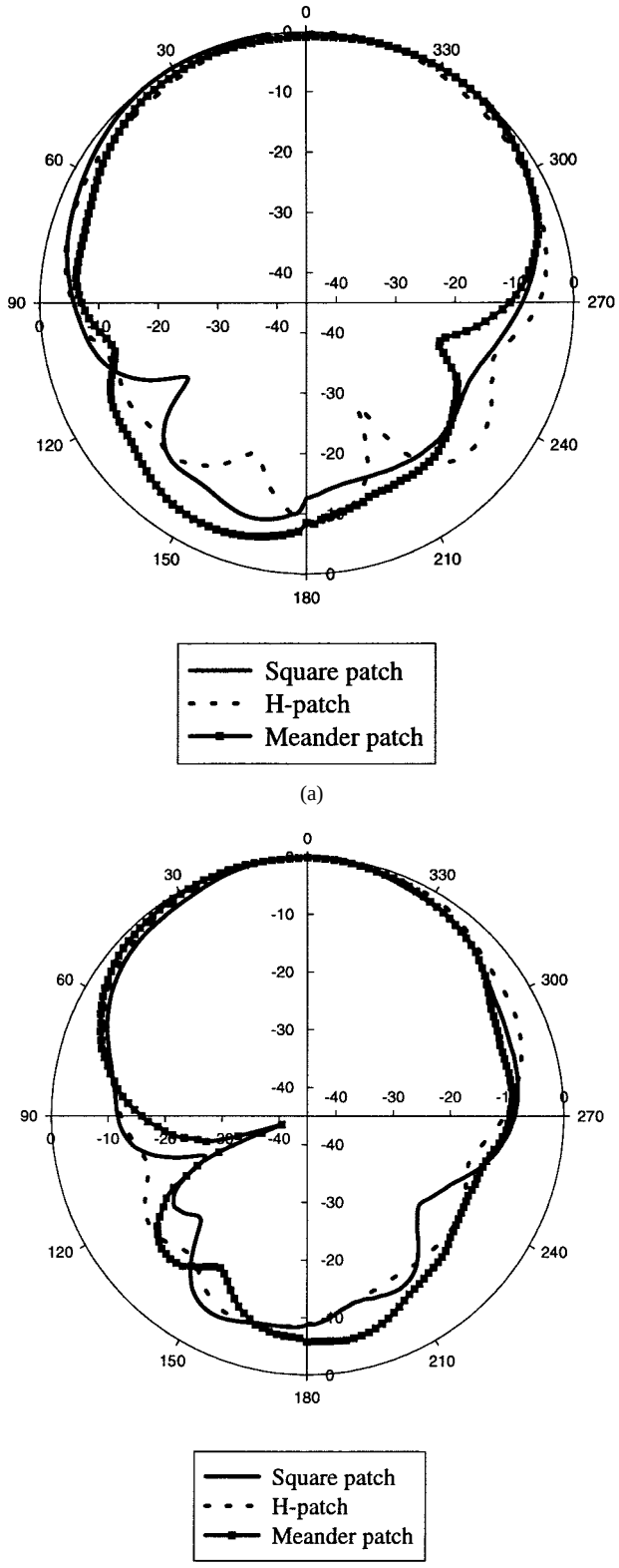

Fig. 9. (a) Measured E-plane of radiation pattern. (b) Measured H-plane of radiation pattern.

gains. In the theoretical calculations for the copper antennas, the loss tangent of the substrate material is $\tan\delta = 10^{-4}$, and the surface resistance R_s for the copper antenna is $0.0261 \cdot (\frac{f}{10^{10}})^{0.5}$ ($R_s = 1.27 \cdot 10^{-2}$ at $f = 2.35$ GHz). For

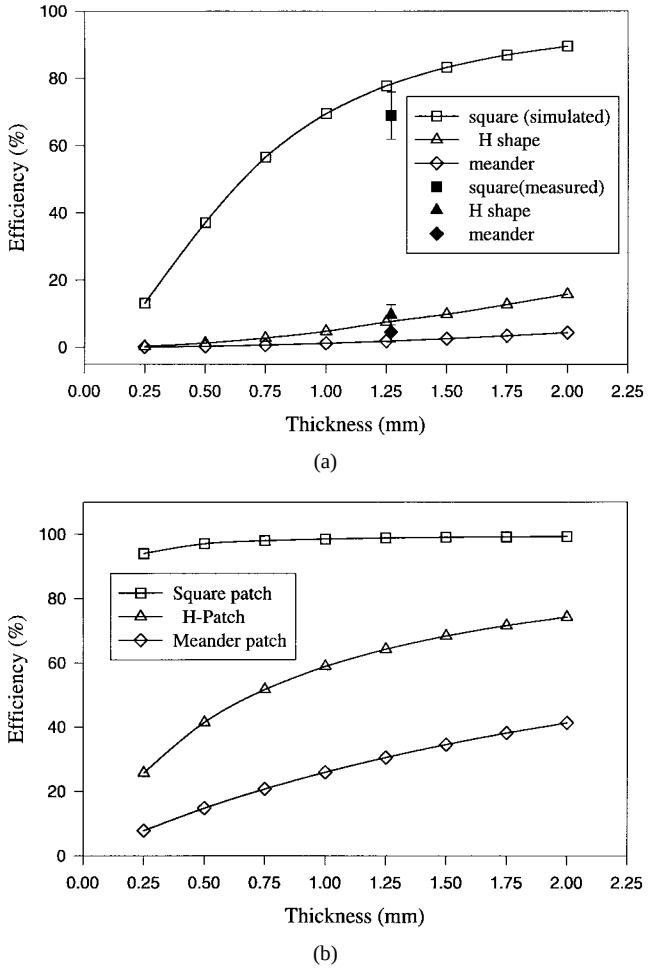

Fig. 10. (a) Efficiency as a function of thickness (copper). (b) Efficiency as a function of thickness (HTS).

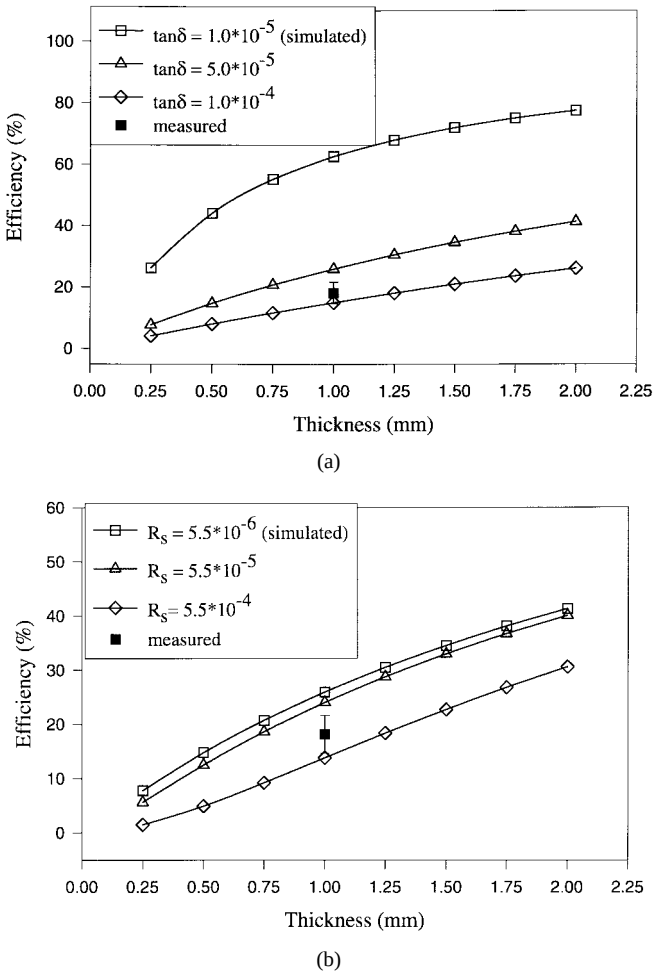

Fig. 11. (a) Efficiency of meander patch against thickness (HTS). (b) Efficiency of meander patch against thickness (HTS).

the HTS antenna the loss tangent of the substrate material is $\tan\delta = 5 \cdot 10^{-5}$ and surface resistance is $10^{-4} \cdot (\frac{f}{10^{10}})^2$ ($R_s = 5.5 \cdot 10^{-6}$ at $f = 2.35$ GHz). The radiation efficiency as a function of frequency for the copper and HTS antennas is shown in Fig. 10. The range of the efficiency for copper meander patch is from 0.3% to 4.4% for the chosen thickness and this is much lower in comparison with conventional patch antennas. However, if HTS thin film is employed for the fabrication of the meander line on the patch the radiation efficiency of the meander patch can be improved significantly. Based on the measured results, the gain of the HTS meander patch with 1.00 mm thickness is 5.5 dB higher than that of the copper meander patch, and the efficiency of the meander patch increases from 4.6% to 18.2%. As can be seen in Fig. 11(a) where the radiation efficiency of the HTS meander patch for various loss tangents is shown, higher radiation efficiency can be further achieved if substrates with lower loss tangent are introduced. Typically, the radiation efficiency of the HTS patch with 1.00 mm substrate thickness could be increased from 15.0% to 62.0% if the loss tangent is reduced from 10^{-4} to 10^{-5}. Furthermore, the quality of the HTS film has also significant impact on radiation efficiency, as illustrated in Fig. 11(b). The measured radiation efficiencies shown in these figures were derived from measured E-plane and H-plane of radiation patterns and the gain which was obtained from a two-antenna measurement method using a dipole as a reference antenna. The measured results are generally in good agreement with the calculated results based on the cavity model.

V. Conclusion

Meander patch antennas fed by microstrip line through an H-shaped aperture have been examined by employing the cavity model for microstrip antenna in conjunction with the full wave simulator *em* and microwave network analyzer. The size of the proposed meander patch is much smaller than that of H-shaped patch and conventional rectangular patch whereas its copolarization pattern is almost the same as that of the two patches. The bandwidth of the meander patch can be widen by introducing parasitic radiation elements and choosing the distances between the radiation elements appropriately. The lower radiation efficiency of the meander patch can be significantly improved if the meander line is made of HTS film.

Acknowledgment

The authors would like to thank Dr. J. S. Hong for valuable discussion and Dr. N. Mustapha, Dr. F. Wellhofer, and Dr.

P. Woodall for their help with the antenna fabrications and production of the superconducting thin films by laser ablation.

REFERENCES

[1] V. Palanisamy and R. Gary, "Rectangular ring and H shaped microstrip antennas—Alternatives to rectangular patch antennas," *Electron. Lett.*, vol. 21, no. 19, pp. 874–876, 1985.
[2] M. J. Lancaster, *Passive Microwave Device Applications of High Temperature*. Cambridge, U.K.: Cambridge Univ. Press, 1997.
[3] L. P. Ivrissimtzis, M. J. Lancaster, T. S. M. Maclean, and N. McN. Alford, "High-gain series fed printed dipole arrays made of high-T_c superconductors," *IEEE Trans. Antennas Propagat.*, vol. 42, pp. 1419–1429, Oct. 1994.
[4] R. C. Hansen, "Superconducting antennas," *IEEE Trans. Aerosp. Electron. Syst.*, vol. 26, pp. 345–355, Mar. 1990.
[5] R. J. Dinger, D. R. Bowling, and A. M. Martin, "A survey of possible passive antenna applications of high-temperature superconductors," *IEEE Trans. Microwave Theory Tech.*, vol. 39, pp. 1498–1509, Sept. 1991.
[6] H. Chaloupka, N. Klein, M. Peiniger, H. Piel, A. Pischke, and G. Splitt, "Miniaturized high-temperature superconductor microstrip patch antenna," *IEEE Trans. Microwave Theory Tech.*, vol. 39, pp. 1513–1521, Sept. 1991.
[7] H. Chaloupka, "High-temperature superconductor antennas: Utilization of low rf losses and nonlinear effects," *J. Superconductivity*, vol. 5, no. 4, pp. 403–416, 1992.
[8] N. Suzuki, K. Itoh, Y. Nagai, and O. Michikami, "Superconductive small antennas made of EuBaCuO thin films," in *Proc. 5th Int. Symp. Superconductivity*, Kobe, Japan, Nov. 1992, pp. 1127–1130.
[9] M. Esa and M. J. Lancaster, "Electrically small high-temperature superconducting symmetrical meander dipole antenna," *Inst. Phys. Conf. Ser.*, no. 148, pp. 1191–1194, 1995.
[10] M. J. Lancaster, H. Y. Wang, and J. S. Hong, "Thin film HTS planar antennas," *IEEE Trans. Appl. Superconductivity*, vol. 8, pp. 168–177, Dec. 1998.
[11] D. M. Pozar and S. D. Targonski, "Improved coupling for aperture-coupled microstrip antennas," *Electron. Lett.*, vol. 27, no. 13, pp. 1129–1131, 1991.
[12] *Sonnet User's Manual*, New York, Sonnet Software Inc.
[13] J. R. James and P. S. Hall, *Handbook of Microstrip Antennas*. London, U.K.: Peter Peregrinus Ltd., 1989.

Hanyang Y. Wang received the M.Eng. degree from Northwestern Polytechnic University, Xian, China, in 1986, and the Ph.D. degree from Heriot-Watt University, Edinburgh, U.K., in 1995.

From 1986 to 1991, he was with the Department of Electronic Engineering of Shandong University, Jinan, China, where he served as an Assistant Lecturer, Lecturer, and Associate Professor. From 1995 to 1997 he was a Senior Research Officer in the Department of Electronic System Engineering, the University of Essex, Colchester, U.K. He is currently a Research Fellow in the School of Electrical and Electronic Engineering, the University of Birmingham, Birmingham, U.K. He is the author of over 40 scientific papers on these topics. His research interests include microwave devices for communications, antennas and antenna array, superconducting antennas, and numerical methods for the solutions of electromagnetic radiation and scattering problems.

Michael J. Lancaster received the B.Sc. (physics) and Ph.D. (nonlinear underwater acoustics) degrees, both from Bath University, Bath, U.K., in 1980 and 1984, respectively.

After leaving Bath University, he joined the Surface Acoustic Wave (SAW) Group at the Department of Engineering Science at Oxford University as a Research Fellow. His research was in the design of new novel SAW devices, including filters and filter banks. In 1987 he became a Lecturer at The University of Birmingham, U.K., in the School of Electronic and Electrical Engineering, lecturing in electromagnetic theory and microwave engineering. Shortly afterward he began the study of the science and applications of high-temperature superconductors working mainly at microwave frequencies. Currently, he heads the Electronic and Materials Devices group as a Reader. His present personal research interests include microwave filters and antennas, as well as the high-frequency properties and applications of a number of novel and diverse materials.

Dr. Lancaster currently serves on the MTT-S International Microwave Symposium Technical Committee.